Solutions of the Taylor-Green Vortex Problem Using High-Resolution Explicit Finite Difference Methods

James R. DeBonis
Inlet and Nozzle Branch
NASA Glenn Research Center
Cleveland, Ohio, 44135

Summary

A computational fluid dynamics code that solves the Compressible Navier-Stokes equations was applied to the Taylor-Green vortex problem to examine the code's ability to accurately simulate the vortex decay and subsequent turbulence. The code, WRLES (Wave Resolving Large-Eddy Simulation), uses explicit central-differencing to compute the spatial derivatives and explicit Low Dispersion Runge-Kutta methods for the temporal discretization. Several spatial differencing schemes were examined. In addition, the affect large-eddy simulation sub-grid scale models is described.

1   Code Description

The code used in this study, WRLES (Wave Resolving Large-Eddy Simulation), is a special purpose large-eddy simulation code that uses high-resolution temporal and spatial discretization schemes to accurately simulate the convection of turbulent structures. The code solves the compressible Favre-filtered Navier-Stokes equations. The code is written entirely in Fortran 90 and utilizes both Message Passing Interface (MPI) libraries[4] and OpenMP compiler directives[3] for parallelization. The code uses a family of explicit Runge-Kutta time stepping schemes written in a general M-stage 2-N storage formulation[7]. Central differencing is used for the spatial discretization because of its non-dissipative properties. This helps ensure the accurate convection of turbulent structures. The central difference stencil is written for an arbitrary stencil size and the spatial discretization can be varied by simply changing the width of the stencil and the coefficients. Standard stencils from 2nd- to 12th-order are included. In addition Dispersion Relation Preserving (DRP) stencils are included in the code: Tam's 7-point scheme, and Bogey & Bailly's 7-, 9- and 13-point schemes [1]. Solution filtering is used to maintain stability. This is a low-pass filter that leaves

the low-wavenumber well-resolved structures untouched and removes the high-wavenumber unresolved structures that can cause instability. For the standard central difference schemes the filters of Kennedy and Carpenter [5] are implemented in the code. Bogey and Bailly developed filters to match their DRP stencils and are included.

2 Case Summary

WRLES solves the compressible form of the Navier-Stokes equations. The following flow conditions were specified to provide an incompressible flow at the proper Reynolds number.

Quantity	Value
Reynolds number, Re	1600
Mach Number, M	0.1
Length, L	0.005 ft.
Temperature, T	530 R

Table 1: Flow conditions

Numerous solutions were run to support the following studies

- Baseline study using the 13 point Bogey and Bailley DRP scheme

- Comparison of numerical schemes: standard 4th (ST04), 8th (ST08) and 12th (ST12) order central differncing and 13pt. DRP scheme (BB13)

- Effect of subgrid-stress model: no model, Smagorinsky model and dynamic Smagorinsky model

The 4-stage, 3rd-order Low Dispersion Runge-Kutta time stepping method of Carpenter and Kennedy[2] was used for all cases. For the baseline and numerical scheme investigations, grid resolution studies were performed using grids of 64^3, 128^3, and 256^3 points. For each differencing scheme and grid, a coefficient that multiplies the effect of the filter was halved until a minimum value was found that provided a stable solution with minimal dissipation. It was found that this minimum filter coefficient was the same for all grid resolutions for a given scheme.

The 64^3 and 128^3 cases were run on a single processor desktop workstation with six cores. The 256^3 cases were run on the NASA Pleaides high performance computing system where 8 processors with 8 cores each were used.

The WRLES code was originally written for the 13 point DRP scheme. The full 13-point stencil is always solved and there is no reduction in work for the low-order schemes. The other schemes are implemented by changing the differencing stencil coefficients and zeroes are used where necessary for the the low-order schemes. For this reason timing information is not reported.
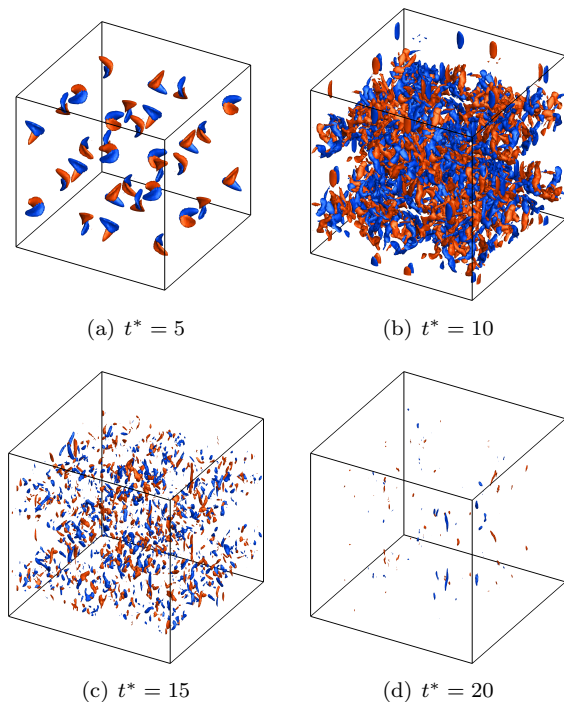
(a) $t^* = 5$ (b) $t^* = 10$

(c) $t^* = 15$ (d) $t^* = 20$

Figure 1: Iso-surfaces of z-vorticity from the BB13 scheme on the 128^3 grid

3 Meshes

The meshes were generated using a Fortran code that also computed the initial conditions. The meshes are regular cartesian meshes of 64^3, 128^3, and 256^3 points. In order to maintain the high-order of accuracy at the boundaries of the domain, additional planes are added beyond $x = \pi L$, $y = \pi L$ and $z = \pi L$ and the periodic boundary conditions are enforced over a range of points adjacent to the boundaries. This insures that all points within the original domain are computed using the full stencil and that the resolution of the scheme is maintained.

4 Results

A baseline set of simulations was performed using the BB13 scheme. Three grid levels were run and a filter coefficient of 0.05 was used for all the cases. Iso-contours of the z-component of vorticity illustrating the vortical motion, transition to turbulence and turbulent decay are shown in figure 1. The change in the integrated kinetic energy over time is shown for all three grid levels in figure 2. Little difference is seen between the grid levels in this plot; although a

(a) complete simulation, $0 < t^* < 20$ (b) close up of $10 < t^* < 20$
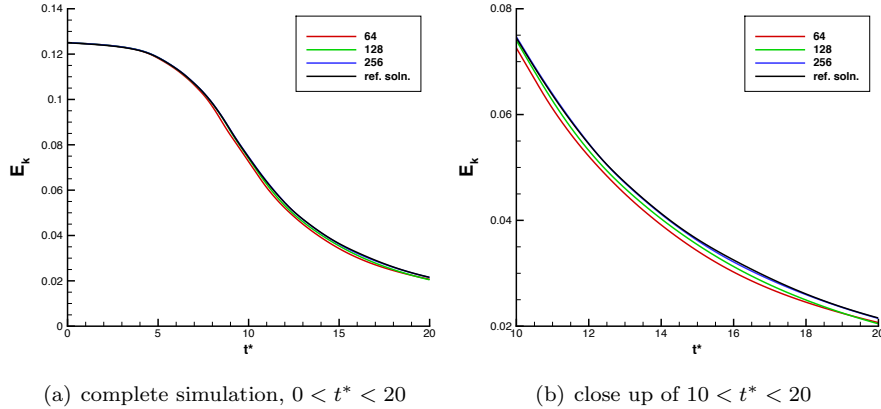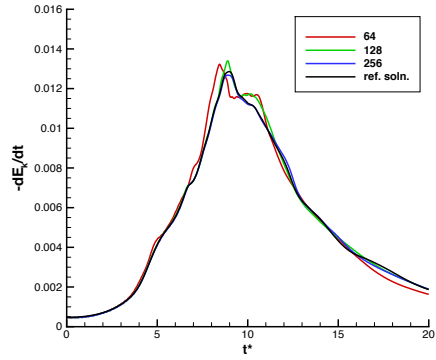
Figure 2: Evolution of kinetic energy

close-up of $10 < t^* < 20$ indicates that the coarser grids contain less energy as time evolves.

Figure 3 shows the evolution of the energy dissipation rate in several forms. The time rate of change of the integrated kinetic energy, $\epsilon = -\frac{\partial E_k}{\partial t}$ is given in figure 3(a). Reasonable agreement with the reference solution[6] is show for all grid levels. The largest discrepancies are at the peak dissipation rates, $7 < t^* < 12$. Here, the accuracy improves with grid resolution and the 256^3 grid is in excellent agreement with the reference solution. The evolution of enstrophy, $\mathcal{E}$, is given in figure 3(b). For incompressible flow $\mathcal{E} = \frac{1}{2}\frac{\rho_0}{\mu}\epsilon$, and one may expect the predictions of $\mathcal{E}$ and ϵ to be similar. However as the figure shows, the enstrophy is more difficult to resolve numerically. The peak enstrophy is severely underpredicted on the coarsest grid. The prediction improves with grid resolution and the enstrophy on the 256^3 grid approaches the correct levels. The primary contribution of the energy dissipation rate, ϵ_1, can be computed from the deviatoric portion of the strain rate tensor (figure 3(c)). This prediction of this quantity is very similar to the prediction of the enstrophy evolution. The other contribution to the energy dissipation rate, ϵ_3, is from the product of pressure and dilatation. For incompressible flow this term should be very small. Figure 3(d) shows that this term is two orders of magnitude smaller than ϵ_1.

Contours of the vorticity norm on the constant x-plane, $x = -\pi L$, at time $t^* = 8$ are shown in figure 4. The vorticity is smeared over a large area at the lowest grid level and the structure is not well defined. At higher grid resolutions, the structure is becomes more defined, less smeared and the peak vorticity level increases. The 256^3 plot closely resembles the reference solution.

A comparision of the four differencing schemes on the three different grid levels is show in figure 5. The kinetic energy dissipation rate and the evolution of enstrophy are shown. These results are consistent with 3. The kinetic energy dissipation is agrees reasonably well for all grid levels and schemes, with the
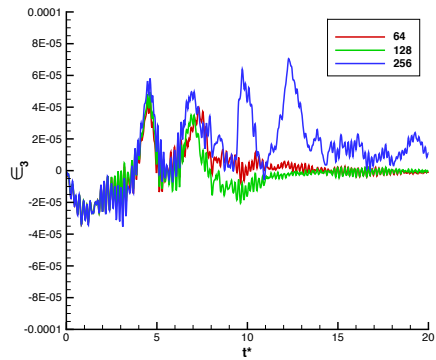
4

(a) time rate of change of integrated kinetic energy, $-\frac{\partial E_k}{\partial t^*}$
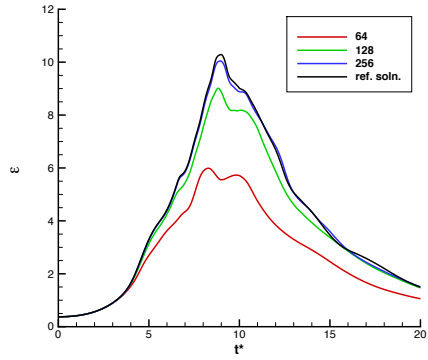
(b) evolution of enstrophy, $\mathcal{E}$
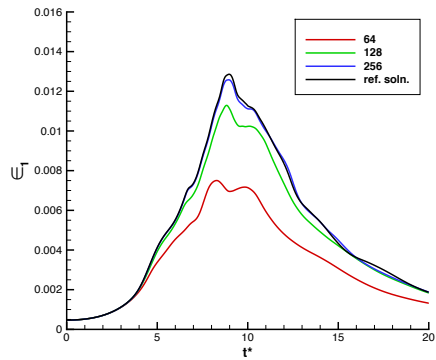
(c) evolution of the deviatoric strain tensor, ϵ_1

(d) evolution of the pressure dilatation, ϵ_3

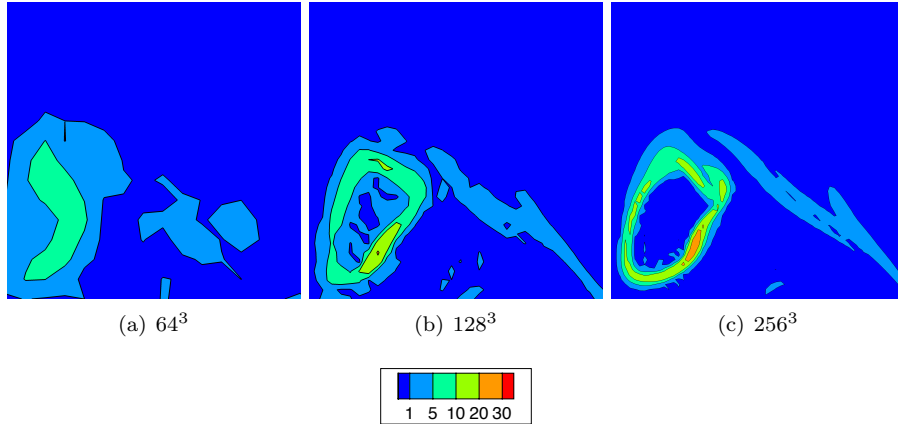Figure 3: Evolution of the energy dissipation rate; comparison of grid resolutions using the BB13 scheme

5

Figure 4: Contours of the vorticity norm, $|\omega|\frac{L}{V_0}$, at $x = -\pi L$ and $t^* = 8$; comparison of grid resolutions using the BB13 scheme

exception of the 4th-order scheme on the 64^3 grid. The enstrophy is under-predicted for all schemes until the 256^3 grid is reached. The ST12 and BB13 schemes, both utilize 13 point stencils and their predictions are very similar with the primary differences occurring at the peak dissipation rates.

To quantify the error in the predicted quantities, the predictions were compared to the reference solution. Linear interpolation was used to compute reference values at the simulation time intervals. The error presented is the L2 error computed over the time period $0 < t^* < 20$. The data is plotted against the grid size, ds, and presented in figure 6 The errors all decrease with grid refinement. But, the relative errors between numerical schemes E_k and $-\frac{\partial E_k}{\partial t}$ vary somewhat from the expected behavior. For example, the 8th-order scheme provides the lowest error in E_k at the 64^3 and 128^3 grid levels. The error in enstrophy behaves as expected with the higher order schemes producing the lowest errors; the 13-point DRP scheme shows slightly lower errors than the standard 12th-order scheme.

Large-eddy simulation sub-grid scale models were examined using the BB13 scheme and the 128^3 grid. The standard Smagorinsky model and the dynamic Smagorinsky model are compared to the no model case. Both sub-grid models perform similarly; increasing the dissipation rate early in the flowfield evolution and reducing the dissipation near the peak dissipation rates. Both models significantly reduce the resolution of enstrophy. The dynamic model produces a jagged $-\frac{\partial E_k}{\partial t^*}$ curve at the peak dissipation rates and also produces slightly higher levels of enstrophy at that location. Both of these effects are due to the backscatter of energy from small to large scales that the dynamic model allows. This was confirmed with a simulation where the backscatter was removed.

(a) 64^3 grid

(b) 64^3 grid

(c) 128^3 grid
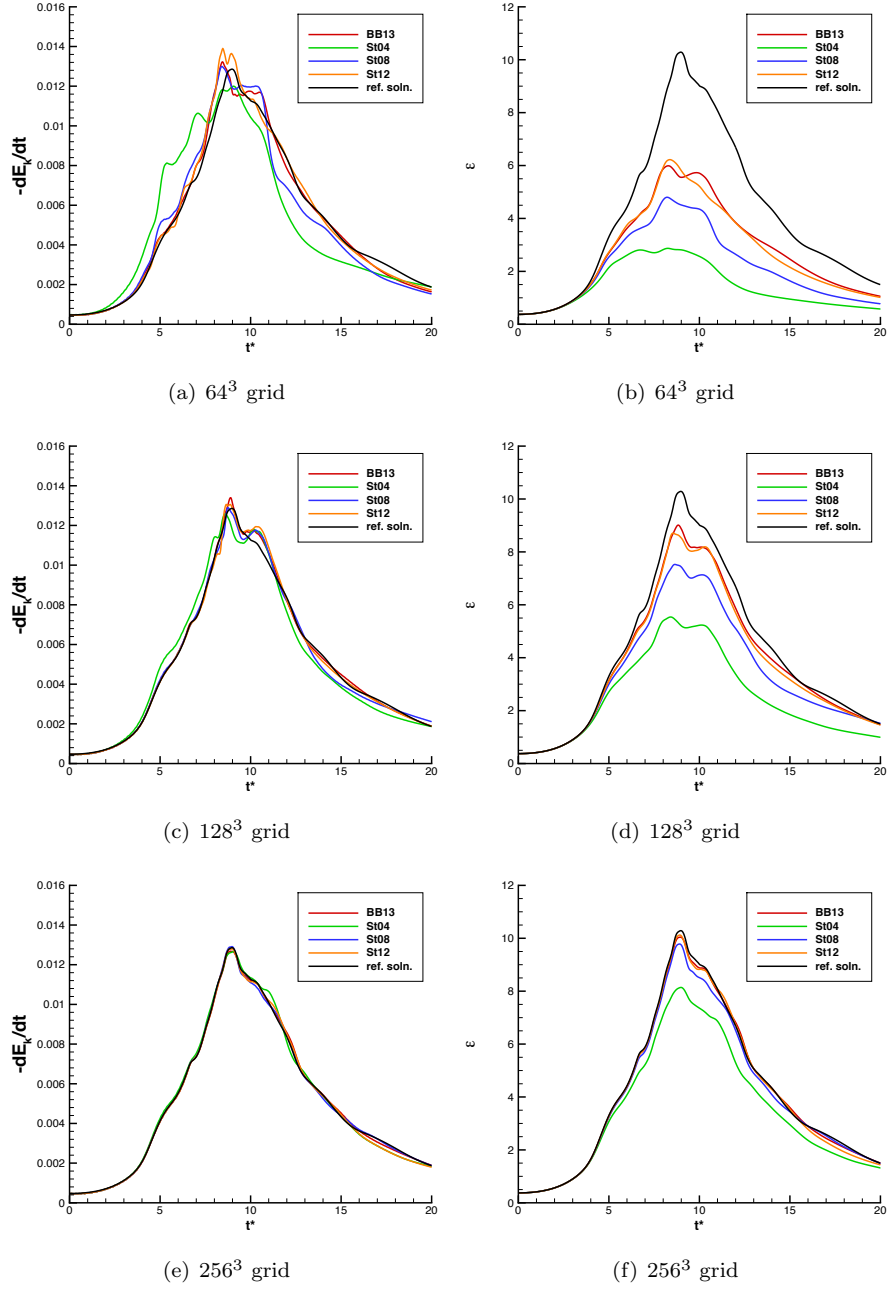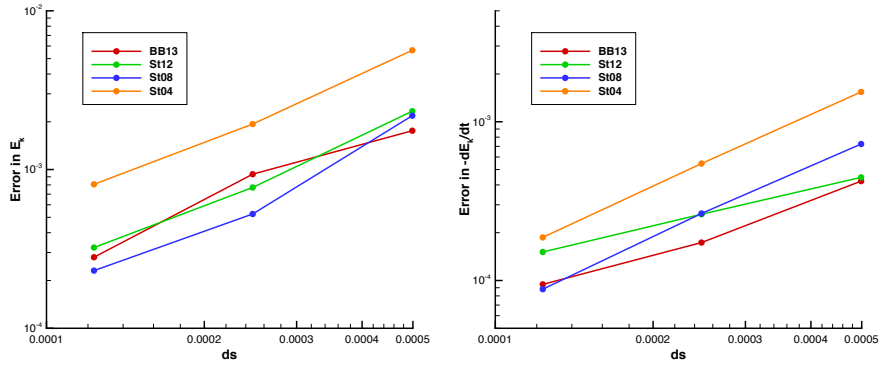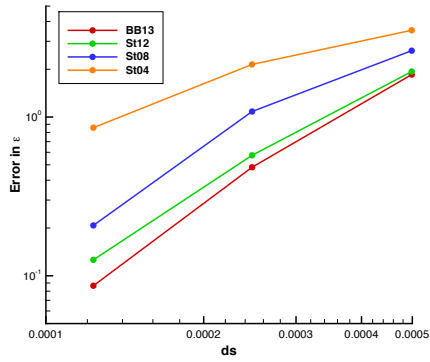
(d) 128^3 grid

(e) 256^3 grid

(f) 256^3 grid

Figure 5: Evolution of the energy dissipation rate; comparison of finite differencing schemes. Left column, time rate of change of integrated kinetic energy, $-\frac{\partial E_k}{\partial t^*}$, right column, evolution of enstrophy, $\mathcal{E}$

(a) Error in E_k

(b) Error in $-\frac{\partial E_k}{\partial t}$

(c) Error in $\mathcal{E}$

Figure 6: Comparison of the average errors

(a) time rate of change of integrated kinetic energy, $-\frac{\partial E_k}{\partial t^*}$
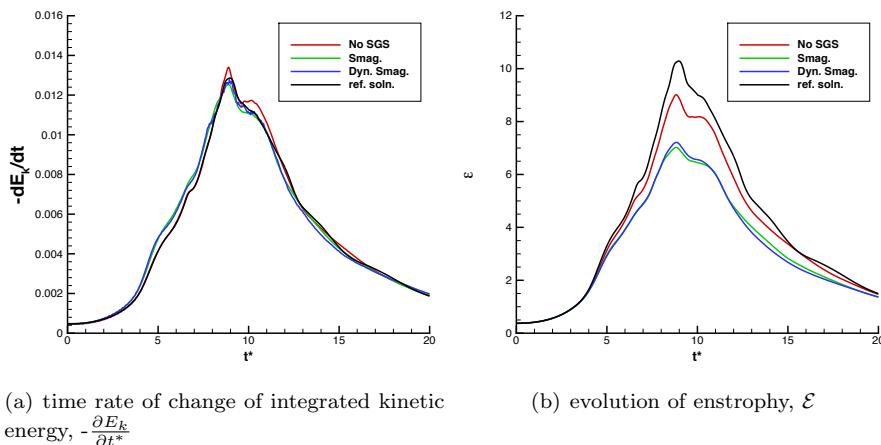
(b) evolution of enstrophy, $\mathcal{E}$

Figure 7: Evolution of the energy dissipation rate; comparison of sub-grid scale models.

References

[1] BOGEY, C., AND BAILLY, C. A Family of Low Dispersive and Low Dissipative Explicit Schemes for Flow and Noise Computations. *Journal of Computational Physics 194* (2004), 194–214.

[2] CARPENTER, M. H., AND KENNEDY, C. A. Fourth-Order 2N-Storage Runge-Kutta Schemes. NASA TM 109112, 1994.

[3] CHAPMAN, B., JOST, G., AND VAN DER PAS, R. *Using OpenMP: Portable Shared Memory Parallel Programming*. The MIT Press, 2007.

[4] FORUM, M. P. I. *MPI: A Message-Passing Interface Standard, Version 2.2* . High Performance Computing Center Stuttgart (HLRS), 2009.

[5] KENNEDY, C. A., AND CARPENTER, M. H. Comparison of Several Numerical Methods for Simulation of Compressible Shear Layers. NASA TP 3484, 1997.

[6] VAN REES, W. M., LEONARD, A., PULLIN, D. I., AND KOUMOUTSAKOS, P. A Comparison of Vortex and Pseudo-Spectral Methods for the Simulation of Periodic Vortical Flows at High Reynolds Numbers. *Journal of Computational Physics 230* (2011), 2794–2805.

[7] WILLIAMSON, J. H. Low-Storage Runge-Kutta Schemes. *Journal of Computational Physics 35* (1980), 48.